Enhanced deflection method for large-curvature problems: Formulation, verification and application to FRP-enabled arches

Z.Y. Xia[1,2], T. Jiang[1*], T. Yu[2]

Abstract

Motivated by a curiosity to explore the behavior of innovative arch structures enabled by the use of fiber-reinforced polymer (FRP) composites, this paper proposes a theoretical model built upon an enhanced formulation of the deflection method, broadening its scope to large-curvature problems. Traditionally, the deflection method approximates curvature as the second-order derivative of deflection, a simplification valid only for small curvatures. This limitation poses a challenge when applying the deflection method to problems involving large curvatures, a characteristic inherent in FRP-enabled arches where significant curvatures arise either initially or due to deformation. The enhanced formulation at the core of the proposed model addresses this challenge by incorporating a circular deflection function. This function posits that each deformed segment of the structural member can be represented by a circular arc, with its curvature and length related to the internal axial force and bending moment at the midpoint section of the segment. This feature facilitates the exact representation of curvature, offering the proposed model a unified approach capable of addressing both small- and large-curvature problems. The paper details the formulation and verification of the theoretical model, with an emphasis on its application to representative cases of FRP-enabled arches.

Keywords: arches; FRP; deflection method; enhanced formulation; large curvatures

[1] Space Structures Research Center, Department of Civil Engineering, Zhejiang University, Hangzhou 310058, China.

[2] Department of Civil and Environmental Engineering, The Hong Kong Polytechnic University, Hong Kong, China.

Corresponding author:

T. Jiang, Space Structures Research Center, Department of Civil Engineering, Zhejiang University, Hangzhou 310058, China. Email: cetjiang@zju.edu.cn

Introduction

Structural members with a longitudinal dimension much greater than their transverse dimensions are commonly referred to as one-dimensional members. These members can be categorized as straight members (e.g., beams and columns) or curvilinear members (e.g., curved beams and arches), depending on the shape of their longitudinal axis (i.e., centroidal axis). In structural analysis, one-dimensional members are commonly characterized by their centroidal axis, which serves as an important reference line for analyzing their behavior.

The deflection method is a widely used technique for analyzing one-dimensional members (Chen and Atsuta, 2007). This method effectively determines the deformed shape of the centroidal axis (i.e., deflection curve) of the member under prescribed loading and boundary conditions. Its effectiveness and accuracy have been demonstrated by successful implementations in straight members (e.g., Shen and Lu, 1983; Jiang and Teng, 2012a; Gao et al., 2021). In this method, the centroidal axis is discretized into many short segments with critical points known as grid points, which are typically located at the ends or midpoint of each segment. This discretization process transforms the continuous deflection curve problem into a discrete initial value problem where numerical procedures are used to solve for the unknown initial values, which are usually the support reactions or displacements at one end of the member.

The deflection method is traditionally based on the small displacement theory, which assumes that the deflection of the member is small compared to its length. This assumption enables simplification of the exact expression for curvature, provided that the centroidal axis of the member is initially straight or nearly so. In these cases, the curvature at any point on the deformed centroidal axis can be approximated as the second-order derivative of the deflection at this point. This simplification allows the deflection and slope at any grid point to be computed from known or assumed information (curvature, slope and deflection) at the previous one or two grid points, depending on the computation scheme employed. As a result, the deflection curve can be generated through a successive process, which involves section analysis at each grid point to determine the corresponding curvature required to proceed to the next grid point. Once the complete deflection curve is generated, boundary conditions are checked and necessary adjustments are repeatedly made to the initial guesses for the unknowns until the updated deflection curve satisfies the prescribed boundary conditions. Detailed descriptions of the conventional deflection method are available in various sources (e.g., Shen and Lu, 1983; Jiang and Teng, 2012b).

The use of simplified curvature representation in the conventional deflection method makes it appropriate for small-curvature problems, or more specifically, straight or slightly crooked one-dimensional members experiencing small displacement. However, its application becomes challenging when dealing with large-curvature problems, where the accuracy of the simplified curvature expression diminishes. Large curvatures in one-dimensional members can arise from geometry-related factors, such as the initial curvatures in arches and curved beams, or from deformation-induced factors, where the large curvatures are developed in initially straight members due to large displacement. In some cases, it can be a combination of both factors.

To address the challenge posed by large-curvature problems, this paper proposes a theoretical model based on an enhanced formulation of the deflection method. The enhanced formulation enables the model to offer a unified approach for handling both small- and large-curvature problems in one-dimensional members. The central insight of the enhanced formulation is that the deformed shape of each segment of the member can be approximated by a circular arc whose curvature and length are related to the internal axial force and bending moment acting on the segment's midpoint section. This assumption allows the deformed centroidal axis to be represented by a continuous curve consisting of a sequence of circular arcs, rather than only discretely by the transverse displacement of the grid points. Therefore, the requirement of exact curvature representation is intrinsically satisfied in the model formulation.

The motivation behind developing the theoretical model largely stems from the authors' curiosity in investigating the behavior of various forms of innovative arch structures enabled by the use of fiber-reinforced polymer (FRP) composites. These structural forms, which are referred to as FRP-enabled arches, are made possible or enhanced by the use of FRP. In their recent review (Xia et al., 2023), the authors identified two sub-categories of FRP-enabled arches: all-FRP arches and FRP-incorporating hybrid arches. The former takes advantage of FRP's lightweight feature, making them ideal for small- or medium-scale applications where construction speed is a key consideration, such as lightweight footbridges and roofs (Sobrino and Pulido, 2002; Caron et al., 2009; Potyrala, 2011; Pyrzowski and Miśkiewicz, 2017; Bell et al., 2020; Liu et al., 2021; Liu et al., 2022). The latter is mainly intended for large-scale applications, such as long-span arch bridges and tunnel linings, where FRP is used in combination with concrete to address the issue of steel corrosion and to achieve excellent mechanical performance (Caratelli et al., 2016; Tang et al., 2020; Lee and Shin, 2010; Dagher et al., 2012; Jiang, 2020; Dong et al., 2022). FRP-enabled arches well exemplify large-curvature problems.

In particular, FRP bending-active arches provide a unique case where the large curvatures are deformation-induced, as they utilize FRP's outstanding elastic deformation ability to derive the arch shape through active bending of initially straight FRP profiles (Caron et al., 2009; Bessini et al., 2019; Habibi et al., 2022; Xie et al., 2023a).

The subsequent sections of this paper are structured as follows. First, the formulation of the theoretical model is presented. This is followed by its verification through comparisons with analytical results of linear elastic arches, serving as an example of large-curvature problems, and numerical results of slender FRP-confined reinforced concrete (RC) columns, serving as an example of small-curvature problems. Next, the verified model is applied to representative cases of FRP-enabled arches, including all-FRP arches and FRP-incorporating hybrid arches, to illustrate large-curvature problems involving both initially-born and deformation-induced curvatures. Comparisons with test results from these cases demonstrate the model's ability to accurately predict the behavior of FRP-enabled arches.

Model Formulation

Discretization Process

Figure 1 illustrates an arch with an arbitrary shape defined by its centroidal axis $y = f(x)$. To discretize the centroidal axis, $n+1$ grid points are used, transforming the original curved axis into n straight segments S_i, where $i \in [1, n]$. The first grid point represents the left support of the arch and serves as the origin of the coordinate system. The last grid point represents the right support and has coordinates $(x_{n+1},\ y_{n+1})$. The two supports are usually at the same height, resulting in $y_{n+1} = 0$. However, non-zero values are also permitted to account for cases where the supports are at different heights. Intermediate grid points can be placed anywhere along the centroidal axis, following two general rules: 1) set a grid point wherever a concentrated force or bending moment is applied; and 2) increase the number of grid points in regions with a sharp change in curvature or a sharp gradient of distributed load. The first rule facilitates model formulation and the second enhances model accuracy. Each segment's initial length $L_{S_i}^0$ and orientation $\theta_{S_i}^0$ relative to the *x*-axis can be easily computed from the grid points' coordinates. Properties of a segment are denoted by symbols with a subscript S_i, and those of a grid point by symbols with a subscript i. Due to the adopted discretization scheme, each intermediate grid point corresponds to two inclination angles $\theta_{i,l}$ and $\theta_{i,r}$, whose initial values are respectively equal to $\theta_{S_{i-1}}^0$ and $\theta_{S_i}^0$. The difference between the two, $\Delta\theta_i = \theta_{S_i}^0 - \theta_{S_{i-1}}^0$, is computed for later use. The initial values of θ_1 and θ_{n+1} are respectively equal to $\theta_{S_1}^0$ and $\theta_{S_n}^0$, which are used to replace the corresponding tangential angles of the original curved arch axis in the calculations.

Deflection Function

The defining feature that sets the model formulation apart from the conventional deflection method is its incorporation of a deflection function. This feature enables the model to provide a unified approach for handling small- and large-curvature problems. The deflection function is derived based on the assumption that, for a small segment, the variations in its internal axial force and bending moment are negligible so that they can be approximated as constants. When the bending moment is constant, the curvature is constant as well, meaning that the deformed segment must take on the shape of a circular arc. Moreover, the axial force being constant means a uniform axial strain along the length of the circular arc, so the change in length of the circular arc is a simple elongation or contraction of the initial segment length. Therefore, the task becomes choosing a representative point on the segment axis and using the axial strain and curvature induced by the internal axial force and bending moment at this point to generate a circular arc that represents the deformed segment shape. To perform this task, the segment midpoint is chosen as the representative point because it well characterizes the average deformation of the segment. An iterative procedure is used to determine the shape of the circular arc, as described below.

Suppose that during a given loading step, the calculation has reached segment S_i (Figure 2a), and the following properties at its left end (i.e., the i th grid point) have been computed: the coordinates (x_i, y_i), the right inclination angle $\theta_{i,r}$, and the internal forces H_i, V_i and M_i. In a general case, the segment is subjected to a variety of external loads, including both concentrated and distributed loads. As per the first discretization rule, the concentrated loads, $H_{ext,i+1}$, $V_{ext,i+1}$ and $M_{ext,i+1}$, are applied at the right end of the segment i (i.e., the $i+1$ th grid point). According to the second discretization rule, the four distrusted loads, q_{x,S_i}, q_{y,S_i}, q_{s,S_i} and q_{R,S_i}, can be simplified as uniform loads with a magnitude equal to their respective value at segment midpoint. These distributed loads are oriented in the horizontal, vertical, arc length and radial directions, respectively, representing different categories of loads, such as pavement load, wind load, gravity, and uniform radial pressure. When acting upon a circular segment, the internal forces caused by q_{x,S_i}, q_{y,S_i}, q_{s,S_i} and q_{R,S_i} at any point on the segment can be calculated by integration along the arc defined by the i th grid point and the point of interest. The expressions for these internal forces are summarized in Table 1, where β denotes the central angle at the point of interest (see Table 1).

Consider the left half of the circular arc. In the first iterative step, the axial force and bending moment at the segment midpoint, $N_{i+\frac{1}{2}}$ and $M_{i+\frac{1}{2}}$, are assumed to be equal to N_i and M_i, respectively, where N_i is the resultant of H_i and V_i in the direction of $\theta_{i,r}$. In this paper, the subscript $i+\frac{1}{2}$ is used to denote properties associated with the midpoint of segment S_i. Section analysis is then performed using the layer method based on the plane section assumption (Jiang and Teng, 2012b). The aim is to find the corresponding strain gradient, defined by the curvature of the neutral axis at the midpoint $\phi_{i+\frac{1}{2}}$ and the axial strain of the centroidal axis at the midpoint $\varepsilon_{i+\frac{1}{2}}$ (Figure 2b). To fulfill this aim, Newton's method is used to iteratively adjust the values of $\phi_{i+\frac{1}{2}}$ and $\varepsilon_{i+\frac{1}{2}}$ until $N_{i+\frac{1}{2}}$ and $M_{i+\frac{1}{2}}$ are balanced (El-Metwally and Chen, 1989). Obviously, the distance between the centroidal axis and the neutral axis $d_{cn} = \varepsilon_{i+\frac{1}{2}}/\phi_{i+\frac{1}{2}}$, so the radius of the circular arc can be expressed as:

$$R_{S_i} = \rho_{S_i} + d_{cn} = 1/\phi_{i+\frac{1}{2}} + \varepsilon_{i+\frac{1}{2}}/\phi_{i+\frac{1}{2}} = \left(1+\varepsilon_{i+\frac{1}{2}}\right)\Big/\phi_{i+\frac{1}{2}} \tag{1}$$

where ρ_{S_i} is the radius of curvature of the neutral axis. Eq. 1 is used to determine the radius of the circular arc. The length of the left half of the circular arc is determined by:

$$\frac{L_{S_i}}{2} = \left(1+\varepsilon_{i+\frac{1}{2}}\right)\frac{L_{S_i}^0}{2} \tag{2}$$

With R_{S_i} and L_{S_i} known, the left half of the arc can be generated with the additional condition that the tangential angle at its left end is $\theta_{i,r}$. The right end of this arc defines a new midpoint whose coordinates are (Figure 2c):

$$\begin{cases} x_{i+\frac{1}{2}} = x_i + \Delta x_{i+\frac{1}{2}} = x_i + R_{S_i} \cdot (\sin(\theta_{i,r}) - \sin(\theta_{i,r} - \beta_{S_i}/2)) \\ y_{i+\frac{1}{2}} = y_i + \Delta y_{i+\frac{1}{2}} = y_i + R_{S_i} \cdot (\cos(\theta_{i,r} - \beta_{S_i}/2) - \cos(\theta_{i,r})) \end{cases} \tag{3}$$

where $\beta_{S_i}/2$ is the corresponding central angle and $= \frac{L_{S_i}}{2}/R_{S_i}$. The tangential angle at the midpoint is:

$$\theta_{i+\frac{1}{2}} = \theta_{i,r} - \beta_{S_i}/2 \tag{4}$$

Now the values of $N_{i+\frac{1}{2}}$ and $M_{i+\frac{1}{2}}$ can be updated:

$$N_{i+\frac{1}{2}} = H_{i+\frac{1}{2}} \cdot \cos(\theta_{i+\frac{1}{2}}) + V_{i+\frac{1}{2}} \cdot \sin(\theta_{i+\frac{1}{2}}) \tag{5a}$$

$$M_{i+\frac{1}{2}} = M_i + H_i \cdot \Delta y_{i+\frac{1}{2}} + V_i \cdot \Delta x_{i+\frac{1}{2}} + \Delta M_{i+\frac{1}{2},q_x} + \Delta M_{i+\frac{1}{2},q_y} + \Delta M_{i+\frac{1}{2},q_s} + \Delta M_{i+\frac{1}{2},q_R} \tag{5b}$$

where

$$H_{i+\frac{1}{2}} = H_i + \Delta H_{i+\frac{1}{2},q_x} + \Delta H_{i+\frac{1}{2},q_s} + \Delta H_{i+\frac{1}{2},q_R} \tag{6a}$$

$$V_{i+\frac{1}{2}} = V_i + \Delta V_{i+\frac{1}{2},q_y} + \Delta V_{i+\frac{1}{2},q_s} + \Delta V_{i+\frac{1}{2},q_R} \tag{6b}$$

In Eqs 5 and 6, the contributions from the distributed loads (i.e., the internal force items with Δ) can be calculated using the expressions provided in Table 1 by setting $\beta =$

$\beta_{S_i}/2$.

The procedure then proceeds to the next iterative step using the updated $N_{i+\frac{1}{2}}$ and $M_{i+\frac{1}{2}}$, and it continues until the distance between the current midpoint and its predecessor obtained in the preceding iterative step is less than $10^{-6}L_{S_i}^0$. Once the left half of the arc is determined, the right half can be easily generated by extending the left half around its center by an angle of $\beta_{S_i}/2$ (Figure 2c). The coordinates of the $i+1$ th grid point can now be determined:

$$\begin{aligned} x_{i+1} &= x_i + \Delta x_i = x_i + R_{S_i} \cdot (\sin(\theta_{i,r}) - \sin(\theta_{i,r} - \beta_{S_i})) \\ y_{i+1} &= y_i + \Delta y_i = y_i + R_{S_i} \cdot (\cos(\theta_{i,r} - \beta_{S_i}) - \cos(\theta_{i,r})) \end{aligned} \quad (7)$$

and the left and right inclination angles at the $i+1$ th grid point are:

$$\theta_{i+1,l} = \theta_{i,r} - \beta_{S_i} \quad (8a)$$

$$\theta_{i+1,r} = \theta_{i+1,l} - \Delta\theta_{i+1} \quad (8b)$$

Finally, the internal forces at the $i+1$ th grid point are obtained:

$$H_{i+1} = H_i + \Delta H_{i+1,q_x} + \Delta H_{i+1,q_s} + \Delta H_{i+1,q_R} + H_{ext,i+1} \quad (9a)$$

$$V_{i+1} = V_i + \Delta V_{i+1,q_y} + \Delta V_{i+1,q_s} + \Delta V_{i+1,q_R} + V_{ext,i+1} \quad (9b)$$

$$M_{i+1} = M_i + H_i \cdot \Delta y_i + V_i \cdot \Delta x_i + \Delta M_{i+1,q_x} + \Delta M_{i+1,q_y} + \Delta M_{i+1,q_s} + \Delta M_{i+1,q_R} + M_{ext,i+1} \quad (9c)$$

where the contributions from the distributed loads can be determined from the expressions provided in Table 1 by setting $\beta = \beta_{S_i}$.

Solution Procedure

The calculations described in the preceding sub-section can be applied sequentially, starting from S_1 and progressing through each intermediate segment until reaching S_n. To initiate the solution procedure, the unknown initial values at the first grid point must be assumed and used in the calculations for S_1. These unknowns correspond to the reaction forces or displacements of the left support, such as H_1, V_1, M_1 and θ_1, depending on the type of support. By making appropriate initial guesses for these unknowns, the calculations can proceed from segment to segment, generating the complete deflection curve. Once the deflection curve is obtained, the boundary conditions at the last grid point need to be examined to ensure their satisfaction. These boundary conditions, which also depend on the type of support, involve the reaction forces and displacements of the right support. Table 2 provides a summary of the unknown initial values and boundary conditions specific to hinged and fixed supports, which are the two most commonly used support types in practice. Each type corresponds to three initial values and three boundary conditions. The numerical examples of this study also encompassed other support types, including rotational springs and vertical sliding hinges. Their properties are also summarized in Table 2.

It is expedient to present first the solution procedure for the simplest case, where the arch is subjected to a single load. In this scenario, the arch can experience failure either due to material limitations (i.e., material failure) or instability (i.e., stability failure), with the likelihood depending largely on its slenderness. Regardless of the failure type, the arch's final deformation state is associated with material failure. Even when stability failure occurs first in the case of slender arches, post-buckling deformation can continue to develop as the load magnitude decreases until it reaches a point where material failure is triggered.

Therefore, the solution procedure adopts an incremental approach using the displacement-control technique. This technique is chosen over the load-control technique because it provides a unified approach to address both stability failure and material failure possibilities. In each incremental step, an increasing displacement value is applied at a selected grid point. The choice of the grid point may vary between incremental steps to ensure that the displacement at the chosen point continues to increase. The goal is to determine the correct load magnitude that induces the prescribed displacement at each step. In this approach, the load magnitude becomes an additional unknown, while the prescribed displacement serves as an additional boundary condition that must be satisfied by the computed deflection curve at the chosen grid point.

The initial step size, denoted as Δf, can be assigned any reasonable small value (e.g., $1/50$ of the ultimate displacement). Initially, the boundary conditions are generally not satisfied by the guessed unknowns. However, the discrepancies between the calculated values and their target values can be used to guide an iterative process that converges toward the correct values of the unknowns. Newton's method is used to implement this iterative process. The process continues until the errors fall within acceptable tolerances, indicating that the solution for the current incremental step has been found. The procedure then proceeds to the next incremental step and continues until material failure occurs.

Material failure is identified through section analysis performed at the midpoint section of each segment. When the calculated axial strain value at any point on the critical section exceeds the material's strain capacity, it indicates that material failure has occurred. In response, the solution procedure is reverted to the previous incremental step and then resumes with a reduced increment of $\Delta f/2$. When material failure is detected again the step size is further halved. This process continues until the step size is eventually reduced to $\Delta f/2^6$, marking the conclusion of the solution procedure.

When the arch is subjected to multiple loads, a loading regime needs to be prescribed to specify the ratios between the load magnitudes. One commonly used regime is proportional loading, where the ratios remain consistent throughout the entire loading process. By prescribing these ratios, the number of additional unknowns associated with the applied loads remains at one. Consequently, the load magnitudes can be determined by solving for the equal number of unknowns and boundary conditions. The remaining steps of the solution procedure follow the same approach as described for the single-load case.

Handling of Intermediate Hinge Joints

Fixed, two-hinged and three-hinged arches are the three basic arch types. So far, the solution procedure has addressed the first two types. However, to apply the procedure to three-hinged arches, a slight modification is required in the model formulation to account for the behavior of the intermediate hinge joint. Consider Figure 2c and assume a hinge joint is located at the segment's right end ($i+1$ th grid point). In this case, Eq. 8 no longer holds, as it is only applicable to rigid connections. Due to the presence of the rotation-free hinge joint, the correlation between the two inclination angles at the

$i+1$ th grid point is lost. Consequently, the right inclination angle, $\theta_{i,r}$, becomes an additional unknown. Simultaneously, a new boundary condition, $M_{i+1} = 0$, is imposed. Therefore, the new unknown $\theta_{i,r}$ can be solved with the other unknowns altogether from the updated boundary conditions using Newton's method.

Handling of Semi-Rigid Connections

Hinged and rigid connections represent idealized connection conditions. In practice, the actual connection condition often lies between these two extremes and requires modeling as semi-rigid connections. One common approach is to model them as rotational springs. Rotational springs can be used to represent both supports and intermediate joints. In either case, the bending moment acting on the spring induces an additional rotation $\omega_i = M_i/k_i$, where k_i is the stiffness of the spring. The initial values and boundary conditions associated with rotational spring supports are summarized in Table 2, capturing the influence of ω_i. Similarly, when an intermediate joint is modeled as a rotational spring, Eq. 8 needs to be modified to incorporate an additional term for ω_i:

$$\theta_{i+1,r} = \theta_{i,r} - \beta_{S_i} - \Delta\theta_{i+1} + \omega_i \tag{10}$$

In fact, hinges and rigid connections can be seen as idealized rotational springs with zero and infinite stiffness magnitudes, respectively. In practice, these idealized spring conditions can be represented by assigning extremely low or extremely high stiffness values. However, hinged and rigid connections are directly represented in the proposed theoretical model instead of modeling them as rotational springs.

The accuracy of the theoretical model is affected by several factors. These include the number of segments used to divide the member, the number of cross-sectional layers adopted in section analysis, and the tolerances set as convergence criteria. In this paper, all numerical examples employed 32 segments and 10^{-6} as the convergence tolerance. The number of cross-sectional layers varied around 200, depending on the cross-sectional configuration. A convergence study showed that further refinement of these factors will not yield any significant effect on the numerical results.

Verification

Comparisons with Analytical Results of Linear Elastic Arches

The theoretical model was verified using the analytical solution derived by Pi and Bradford for linear elastic arches (Pi and Bradford, 2009). Their solution represents a significant advancement over classical elastic arch theories (e.g., Timoshenko and Gere, 1963), as it accounts for the effect of pre-buckling deformations on the displacement and geometric stiffness of the arch. This consideration is particularly important for shallow arches, where pre-buckling deformations significantly influence the arch's buckling behavior (Pi and Trahair, 1998).

The solution of Pi and Bradford (2009) is concerned with the specific loading scenario of elastic circular arches subjected to a uniform radial pressure (Figure 3a). In classical arch theories, this loading scenario results in a compression line coinciding with the arch's centroidal axis. This implies a pure concentric compression stress state of the arch, neglecting the axial deformation caused by the axial compression force. As a result, the predicted buckling mode according to classical arch theories is bifurcation buckling (Timoshenko and Gere, 1963). However, when the effect of axial deformation is considered, the compression line deviates from the centroidal axis as the applied radial pressure increases, introducing bending moments to the arch. This deviation can lead to the arch buckling in either a symmetric snap-through mode or an anti-symmetric bifurcation mode (Pi and Bradford, 2009), as illustrated in Figs. 3b and 3c, respectively. The dominant buckling mode depends on factors such as arch slenderness, shallowness, and level of end restraint.

In the study of Pi and Bradford (2009), the supports of the arch were represented by two elastic rotational springs of equal stiffness, providing symmetrical restraint to the arch. The level of end restraint was indicated by the dimensionless flexibility of the rotational springs α, which was defined as the ratio of the flexural rigidity per arch length to the stiffness of the rotational springs. This parameter can be assigned any value between zero and infinity to represent different levels of end restraint.

Figure 4 presents a comparison between the load–deflection curves at arch crown, as predicted by the theoretical model and the analytical solution of Pi and Bradford (2009). These curves trace the variation of the normalized applied pressure $q_R R/N_{E2}$ as the normalized vertical displacement of the arch crown v_0/f increases, where R and f are respectively the radius and rise of the arch, v_0 is the vertical displacement of the arch crown, and N_{E2} is the second mode flexural buckling load of a pin-ended column with equal rotational end restraints and having the same length as the arch (Pi and Bradford, 2009). Two representative sets of arches were considered, one with α =0.1 and the other with α =1.5, to represent a relatively high and a relatively low level of end restraint, respectively. Each set covered four cases, each corresponding to a specific value of a geometrical parameter λ introduced by Pi and Bradford (2009). This parameter reflects both the slenderness and shallowness of the arch and has a significant influence on its buckling behavior.

The λ value used for Figure 4a is a boundary value predicted by the analytical solution. Under this specific λ, the postbuckling descending branch of the load–deflection curve for the arch with $\alpha = 1.5$ reduces to a single point. That is, it demarcates the boundary between stability and instability for $\alpha = 1.5$: any λ greater than this boundary value leads to the occurrence of stability failure, while any lesser λ eliminates the possibility of stability failure and is thus associated with a monotonically increasing load–deflection curve. Similarly, the λ value used for Figure 4b is the counterpart boundary value for $\alpha = 0.1$. Under this λ, due to the lower level of end restraint, the arch with $\alpha = 1.5$ fails by instability in the symmetrical snap-through mode and exhibits a postbuckling descending branch on its load–deflection curve. The λ value used for Figure 4c is such that the anti-symmetric bifurcation mode is triggered for the arch with $\alpha = 1.5$, although the dominant buckling mode remains the snap-through mode. The portion corresponding to the anti-symmetric deformation phase is defined by the two solid symbols on the load–deflection curve. In Figure 4d, λ is further increased to such a value that bifurcation buckling becomes the dominant buckling mode for the arch with $\alpha = 1.5$. It should be noted that a perturbation is needed for the theoretical model to excite the anti-symmetric buckling mode. This perturbation was introduced as a small bending moment with a magnitude of $10^{-3} N_{E2} f$ applied at the arch crown.

Evidently, the predictions by the theoretical model match those by the analytical solution very well, except for the case shown in Figure 4a with $\alpha = 0.1$. The discrepancy observed for this particular case is believed to arise from an inadvertent mistake made by Pi and Bradford (2009) in using the value of N_{E2} when normalizing the applied pressure for this case. Pi and Bradford (2009) claimed that for convenience a fixed value of N_{E2}, which was determined from the condition $\alpha = 1.5$, was consistently used for all cases considered in Figure 4, despite the fact that N_{E2} varies with α. However, it appears that this rule was not followed by Pi and Bradford (2009) when preparing the plot for this particular case, where it is believed that the value of N_{E2} was actually determined from the condition α =0.1. When this N_{E2} value is used, the predicted normalized load–deflection curve for this case becomes the additional dashed curve shown in Figure 4a, removing the previously observed discrepancy.

Comparisons with Numerical Result of Slender FRP-Confined RC Columns

The theoretical model's capability to address small-curvature problems is demonstrated through comparisons with the numerical results of a column model previously developed by the second author (Jiang and Teng, 2012b). This column model is based on the conventional deflection method and has been verified in Jiang and Teng (2012b), where its accuracy for slender RC columns and FRP-confined RC columns is also shown.

The numerical verification is based on referencing four slender FRP-confined circular RC columns tested by Tao et al. (2004), using the properties of these columns as inputs for both models. These columns, measuring 150 mm in diameter and 1260 mm in height, were reinforced with four 12 mm longitudinal steel bars and enveloped in a circumferential carbon FRP (CFRP) wrap with a nominal thickness of 0.34 mm. The concrete cover to the longitudinal steel reinforcement was 21 mm. All columns were pin-ended and subjected to equal load eccentricities at the two ends. The four columns were labeled C1-1R, C1-2R, C1-3R, and C1-4R, respectively, distinguished by their nominal load eccentricities (0 mm, 50 mm, 100 mm, and 150 mm). The material properties are as follows. The unconfined concrete strength was 48.2 MPa and the yield strength of the longitudinal steel reinforcement was 388.7 MPa. The CFRP wrap had an elastic modulus of 255 GPa and a hoop rupture strain of 1.32%. More details of these tests can be found elsewhere (Jiang and Teng, 2012b; Tao et al., 2004).

The load–deflection responses of the four columns were simulated using both the theoretical model and the column model of Jiang and Teng (2012b), with both models incorporating the same stress–strain models. Teng et al.'s (2009) design-oriented model, which is a refined version of Lam and Teng's (2003) model, was employed to characterize the compressive stress–strain behavior of FRP-confined concrete, while the tensile strength of concrete was ignored. The longitudinal steel reinforcement was assumed to possess an elastic-perfectly plastic stress–strain curve.

Figure 5 illustrates a comparison between the load–deflection curves at column mid-height, as predicted by the two models. Following the approach of Jiang and Teng (2012b), all cases were modeled with an additional eccentricity of 7.5 mm added to the nominal load eccentricity. The two sets of theoretical curves exhibit excellent agreement, demonstrating the capability of the theoretical model in addressing small-curvature problems.

Application to FRP-enabled Arches

FRP Bending-Active Arches

Bending-active arches are a unique category of arch structures. They derive their curved shape from elastic bending of initially straight members (Lienhard et al., 2013; Xie et al., 2023b; Xie et al., 2024). FRP bending-active arches are suitable for use as rapidly assembled crossing bridges and supporting frames for temporary structures (Xia et al., 2023; Caron et al., 2009; Bessini et al., 2019; Habibi et al., 2022).

The tests conducted by Xie et al. (2023a) were employed as an example of all-FRP arches to validate the theoretical model. In their tests, the arch specimens were bent from straight CFRP strips with a cross section of 48.5 mm by 1.40 mm. During the bending process, the supports of the specimen allowed free rotation in the plane of the arch axis. Once the arch specimen was bent into place, the supports were transitioned to a clamped condition before receiving a concentrated load vertically applied at the arch crown. A total of 16 arch configurations were tested, with the main variables being the strip length and the span ratio (the ratio of arch span to strip length). The strip length was either 1.6 m or 2.0 m, each covering four span ratios (0.6, 0.7, 0.8 and 0.9). The CFRP had a flexural modulus of 127.5 GPa and a density of 1620 kg/m^3.

Figure 6 displays a comparison between the experimental and predicted load–deflection curves at arch crown for all specimens. Each predicted curve was terminated when its predicted load aligned with the load at the final point of the corresponding experimental curve. As only the symmetrical snap-through buckling mode was observed in the tests, the modeling work simplified the arch specimen by considering only half of its original configuration. As a result, the support condition at the arch crown was modeled as a vertical sliding hinge (see Table 2). Additionally, the influence of gravity was considered, as it proved significant due to the large flexibility of the arch specimens. As illustrated in Figure 6, the predicted load–deflection curves closely align with their experimental counterparts.

For illustrative purposes, Figure 7 provides a further comparison between the experimental and predicted deformed shapes of Specimen L16SR60. This specimen had a length of 1.6 m and a span ratio of 0.6. The comparisons were made at three representative states (State I, State II and State III), which correspond to the initial point, peak point and valley point of the load–deflection curve, respectively. Evidently, the theoretical model successfully reproduces the deformed shapes, demonstrating its accuracy in capturing the behavior of the arch specimens.

Concrete-filled FRP Tubular (CFFT) Arches

CFFT arches are a promising form of FRP-incorporating hybrid arch, offering a combination of strength, ductility and durability. This desirable behavior is attributed to the confinement, reinforcement and protection provided to the concrete core by the FRP tube. The theoretical model is further validated using two series of tests on CFFT arches conducted by the same research group (Dagher et al., 2012; Majeed et al., 2021). Both test series focused on circular arches with a circular cross-section, subjecting them to a concentrated load vertically applied at the arch crown. The geometrical and material properties of the CFFT arches in both test series are summarized in Table 3.

The first test series (Dagher et al., 2012) involved four nominally identical CFFT arches (A1, A2, A3 and A4) subjected to monotonic loading. These arch specimens were cast into RC footings at both ends, with the footings being pin-supported on the laboratory floor. For each arch specimen, the FRP tube comprised an inner layer of glass fibers and two outer layers of carbon fibers. By using different fiber orientations for the inner and outer layers, the resulting FRP tube exhibited significant stiffness in both the longitudinal and hoop directions. In the theoretical model, each RC footing was simplified as a rigid link, and the FRP tube's behavior was assumed to be linear elastic in both the longitudinal and hoop directions. The interaction between the tube's behaviors in these two directions was neglected in the analysis.

In the absence of test data, the elastic modulus and tensile strength of concrete were determined based on its compressive strength in accordance with the ACI standard (ACI 318-19, 2019). For consistency, Teng et al.'s (2009) model was again employed to describe the stress–strain behavior of FRP-confined concrete in compression. It should be noted that Teng et al.'s (2009) model requires the input of the FRP rupture strain. This value was assumed to be 2% as it was not reported in the original literature (Dagher et al., 2012). Varying the rupture strain in the range of 1~3% showed a negligible influence on the model predictions because the failure of the arch specimens was not due to the rupture of the FRP tube in the hoop direction. The stress–strain curve of concrete in tension was assumed to be linear before cracking. The tension-stiffening effect was accounted for using the model proposed by Collins and Mitchell (1997). This model is a modification of Vecchio and Collins's (1986) tension-stiffening model and has demonstrated a good predictive capability concerning moment-curvature relationships for CFFT flexural members in previous studies (Bannon et al., 2009; Fam, 2000). Full composite action was assumed between the FRP tube and the concrete core. Additionally, only half of the arch specimen was considered due to symmetry.

Figure 8a compares the experimental and predicted load–deflection curves at arch crown. Notably, Specimens A1 and A2 exhibited a less stiff initial response than

Specimens A3 and A4. Dagher et al. (2012) attributed this difference to accidental damage prior to testing and initial imperfections. Therefore, the load–deflection curves of Specimens A3 and A4 are considered to better represent the true behavior of the arch specimens. These two curves are closely matched by the predicted curve. Dagher et al. (2012) reported that the failure of all arch specimens was due to longitudinal rupture of the FRP tube in the tension face, directly below the point of load application. Hence, the predicted curve terminates when the FRP tube reaches its longitudinal rupture strain.

The second test series (Majeed et al., 2021) exclusively focused on a fixed CFFT arch with a more slender configuration. The FRP tube used in this test consisted of two layers of glass fibers, with each layer having a distinct fiber angle. The failure mode observed in this specimen was consistent with the one observed in the first test series. The modeling procedure for this specimen was similar to that used for the first test series, except for a variation in the support condition. As illustrated in Figure 8b, the theoretical model accurately predicts the load–deflection response of this specimen.

Conclusions

This paper has been concerned with the formulation, verification and application of a theoretical model for one-dimensional members. Originally developed to address the challenges posed by large-curvature problems encountered in FRP-enabled arches, the model's versatility enables its application to the broader range of general one-dimensional members. The work presented in this paper allows the following conclusions to be drawn:

1) The theoretical model is built upon an enhanced formulation of the deflection

method. Its defining feature is the incorporation of a circular deflection function, which posits that each segment of the deformed centroidal axis can be represented by a circular arc whose curvature and length are related to the internal axial force and bending moment acting on the segment's midpoint section. This feature facilitates the exact representation of curvature, distinguishing the proposed model from the conventional deflection method, where the simplified representation of curvature as the second-order derivative of deflection is valid only for small curvatures. Therefore, the proposed model represents a significant improvement over the conventional deflection method in that it offers a unified approach to address both small- and large-curvature problems.

2) Model verification was carried out through comparisons with both analytical and numerical results from the literature. The analytical verification focused on a large-curvature problem of linear elastic arches, while the numerical verification employed a small-curvature problem of slender FRP-confined RC columns, incorporating material non-linearity. The verification results demonstrated the correct implementation of the theoretical model and its equal capability in handling small- and large-curvature problems.

3) The performance of the theoretical model was evaluated against representative test results from FRP-enable arches, comprising two sub-categories: all-FRP arches exemplified by FRP-bending active arches and FRP-incorporating hybrid arches exemplified by CFFT arches. In the case of FRP-bending active arches, the large curvatures were induced by deformation, whereas in CFFT arches, the large curvatures were inherent in their initial configuration. The theoretical model

demonstrated excellent accuracy in predicting the behavior of arches in both sub-categories, regardless of the source of the large curvatures.

Acknowledgments

The PolyU-ZJU Joint PhD Program is gratefully acknowledged for enabling the first author's PhD journey under the joint supervision of the second and third authors.

Declaration of Conflicting Interests

The authors declare that there is no conflict of interest.

Funding

The authors are grateful for the financial support provided by the National Natural Science Foundation of China (Project No.: 51778569) and the Hong Kong Research Grants Council (Project No.: T22-502/18-R).

References

ACI 318-19. (2019) Building Code Requirements for Structural Concrete. Farmington Hills, Michigan: American Concrete Institute (ACI), USA.

Bannon DJ, Dagher HJ and Lopez-Anido RA. (2009) Behavior of inflatable rigidified composite arch bridges. *Composites & Polycon*: 15-17.

Bell M, Fick D, Ament R, et al. (2020) The use of fiber-reinforced polymers in wildlife crossing infrastructure. *Sustainability* 12(4): 1557.

Bessini J, Lazaro C, Casanova J, et al. (2019) Efficiency-based design of bending-active tied arches. *Engineering Structures* 200: 109681.

Caratelli A, Meda A, Rinaldi Z, et al. (2016) Precast tunnel segments with GFRP reinforcement. *Tunnelling and Underground Space Technology* 60: 10-20.

Caron JF, Julich S and Baverel O. (2009) Selfstressed bowstring footbridge in FRP.

Composite Structures 89(3): 489-496.

Chen WF and Atsuta T. (2007) *Theory of Beam-columns*: J. Ross Publishing.

Collins MP and Mitchell D. (1997) *Prestressed Concrete Structures,* Toronto and Montreal, Canada: Response Publications.

Dagher HJ, Bannon DJ, Davids WG, et al. (2012) Bending behavior of concrete-filled tubular FRP arches for bridge structures. *Construction and Building Materials* 37: 432-439.

Dong ZQ, Liu ZQ, Wu G, et al. (2022) Study on mechanical properties of seawater sea-sand coral aggregate concrete-filled BFRP tubular arches. *Advances in Structural Engineering* 25(9): 1851-1865.

El-Metwally SE and Chen WF. (1989) Load-deformation relations for reinforced concrete sections. *Structural Journal* 86(2): 163-167.

Fam AZ. (2000) Concrete-filled Fibre-reinforced Polymer Tubes for Axial and Flexural Structural Members. Manitoba, Canada: The University of Manitoba.

Gao K, Xie H, Li Z, et al. (2021) Study on eccentric behavior and serviceability performance of slender rectangular concrete columns reinforced with GFRP bars. *Composite Structures* 263: 113680.

Habibi T, Rhode Barbarigos L and Keller T. (2022) Fiber-polymer composites for permanent large-scale bending-active elastica beams. *Composite Structures* 294: 115809.

Jiang S. (2020) Hybrid FRP-concrete-steel Double-skin Tubular Truss Bridge: Design, Construction and Testing. Queensland, Australia: The University of Queensland.

Jiang T and Teng JG. (2012a) Slenderness limit for short FRP-confined circular RC columns. *Journal of Composites for Construction* 16(6): 650-661.

Jiang T and Teng JG. (2012b) Theoretical model for slender FRP-confined circular RC columns. *Construction and Building Materials* 32: 66-76.

Lam L and Teng JG. (2003) Design-oriented stress–strain model for FRP-confined concrete. *Construction and Building Materials* 17(6-7): 471-489.

Lee GP and Shin HS. (2010) A numerical study on feasibility of the circled fiber reinforced polymer (FRP) panel for a tunnel lining structure. *Journal of Korean Tunnelling and Underground Space Association* 12(6): 451-461.

Lienhard J, Alpermann H, Gengnagel C, et al. (2013) Active bending, a review on structures where bending is used as a self-formation process. *International Journal of Space Structures* 28(3-4): 187-196.

Liu SY, Zhang ZY, Xue X, et al. (2022) Deformation properties of arched glass fiber reinforced plastics structure under static load: Considering the soil cover and rise-span ratio. *Advances in Structural Engineering* 25(6): 1254-1267.

Liu T, Feng P, Wu Y, et al. (2021) Developing an innovative curved-pultruded large-scale GFRP arch beam. *Composite Structures* 256: 113111.

Majeed HS, Davids WG and Walton HJ. (2021) Efficient second-order nonlinear finite-element simulation of concrete-filled FRP tubular arches. *Structures* 34: 3738-3749.

Pi YL and Bradford M. (2009) Non-linear in-plane postbuckling of arches with rotational end restraints under uniform radial loading. *International Journal of Non-Linear Mechanics* 44(9): 975-989.

Pi YL and Trahair NS. (1998) Non-linear buckling and postbuckling of elastic arches. *Engineering Structures* 20(7): 571-579.

Potyrala PB. (2011) Use of Fibre Reinforced Polymeromposites in Bridge Construction. State of the Art in Hybrid and All-composite Structures. Catalonia, Spain: Polytechnic University of Catalonia.

Pyrzowski Ł and Miśkiewicz M. (2017) Modern GFRP composite footbridges. *In Proc., "Environmental Engineering" 10th International Conference.* Vilnius Gediminas Technical University, Ottawa, Canada, 1-8.

Shen ZY and Lu LW. (1983) Analysis of initially crooked, end restrained steel columns. *Journal of Constructional Steel Research* 3(1): 10-18.

Sobrino JA and Pulido MDG. (2002) Towards advanced composite material footbridges. *Structural Engineering International* 12(2): 84-86.

Tang ZX, Zhou YZ, Feng J, et al. (2020) Blast responses and damage evaluation of concrete protective arches reinforced with BFRP bars. *Composite Structures* 254: 112864.

Tao Z, Teng JG, Han LH, et al. (2004) Experimental behaviour of FRP-confined slender RC columns under eccentric loading. *In Proc., Proceedings, Second International Conference on Advanced Polymer Composites for Structural Applications in Construction.* University of Surrey, Guildford, UK, 203-212.

Teng JG, Jiang T, Lam L, et al. (2009) Refinement of a design-oriented stress–strain model for FRP-confined concrete. *Journal of Composites for Construction*

13(4): 269-278.

Timoshenko SP and Gere JM. (1963) *Theory of Elastic Stability,* New York, USA: McGraw-Hill International Book Company.

Vecchio FJ and Collins MP. (1986) The modified compression-field theory for reinforced concrete elements subjected to shear. *ACI Journal* 83(2): 219-231.

Xia ZY, Jiang T and Yu T. (2023) Innovating arch structures with fiber-reinforced polymer composites: A review. *Advances in Structural Engineering* 26(13): 2341-2358.

Xie EL, Jiang T, Xia ZY, et al. (2023a) Postbuckling behavior of FRP bending-active arches subjected to a central point load. *Journal of Composites for Construction* 27(5): 04023039.

Xie EL, Song YX, Zhang PF, et al. (2024) FRP bending-active gridshells: Numerical simulation and model test. *Structures* 61: 106064.

Xie P, Lam L and Jiang T. (2023b) Compressive behavior of GFRP tubes filled with self-compacting concrete. *Journal of Composites for Construction* 27(1): 04022103.

Table 1. Internal forces caused by distributed loads.

Diagram	Load type	Horizontal force	Vertical force	Bending moment
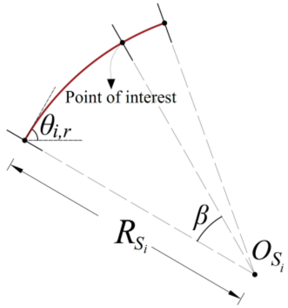	q_{x,S_i}	$q_{x,S_i}R_{S_i}(\cos(\theta_{i,r}-\beta)-\cos(\theta_{i,r}))$	0	$\frac{1}{2}q_{x,S_i}R_{S_i}^2((\cos(\theta_{i,r}-\beta)-\cos(\theta_{i,r}))^2$
	q_{y,S_i}	0	$q_{y,S_i}R_{S_i}(\sin(\theta_{i,r}-\beta)-\sin(\theta_{i,r}))$	$\frac{1}{2}q_{y,S_i}R_{S_i}^2(\sin(\theta_{i,r})-\sin(\theta_{i,r}-\beta))^2$
	q_{s,S_i}	0	$-q_{s,S_i}\beta R_{S_i}$	$q_{s,S_i}R_{S_i}^2(\cos(\theta_{i,r}-\beta)-\cos(\theta_{i,r})-\beta\sin(\theta_{i,r}-\beta))$
	q_{R,S_i}	$q_{R,S_i}R_{S_i}(\cos(\theta_{i,r}-\beta)-\cos(\theta_{i,r}))$	$q_{R,S_i}R_{S_i}(\sin(\theta_{i,r}-\beta)-\sin(\theta_{i,r}))$	$q_{R,S_i}R_{S_i}^2(1-\sin(\theta_{i,r})\sin(\theta_{i,r}-\beta)-\cos(\theta_{i,r})\cos(\theta_{i,r}-\beta))$

Table 2. Unknown initial values and boundary conditions of typical types of supports.

Support type	Horizontal load	Vertical load	Bending moment	Horizontal displacement	Vertical displacement	Rotation
Fixed	Unknown	Unknown	Unknown	0	0	0
Hinged	Unknown	Unknown	0	0	0	Unknown
Rotational spring	Unknown	Unknown	Unknown	0	0	moment/spring stiffness
Vertical sliding hinge	Unknown	0	Unknown	0	Unknown	0

Table 3. Geometrical and material properties of CFFT arches.

Test series	Arch span (m)	Arch rise (m)	Arch radius (m)	Boundary condition	Section diameter (mm)	Concrete strength (MPa)	FRP tube wall thickness (mm)	FRP in longitudinal direction		FRP in hoop direction	
								Elastic modulus (GPa)	**Rupture Strain** (%)	**Elastic modulus** (GPa)	**Rupture Strain** (%)
1st	6.71	2.10	3.96	Hinged	300	27	2.5	42.7	1.70	14.3	-
2nd	6.1	1.22	3.28	Fixed	110	25	2	13.8	2.27[a]	19.4	1.93[a]

Note: [a] These rupture strain values were determined based on the longitudinal and hoop FRP strengths reported in Majeed et al. (2021), assuming the tested coupons were linear elastic.

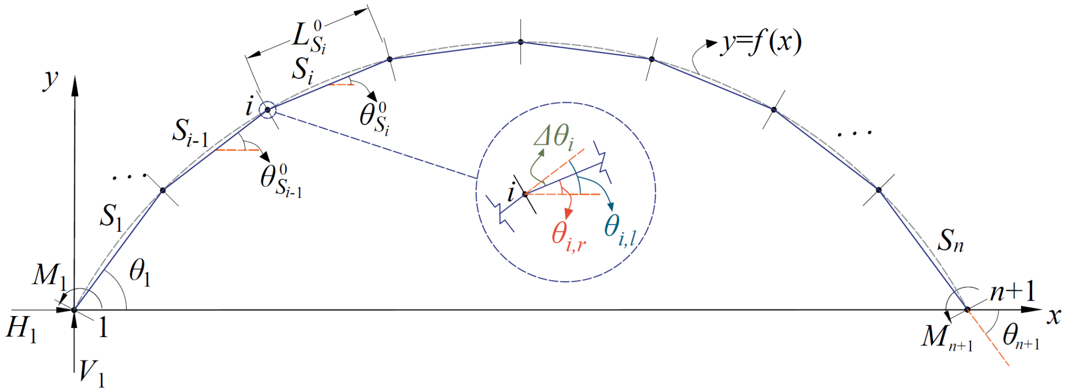

Figure 1. Schematic of the theoretical model.

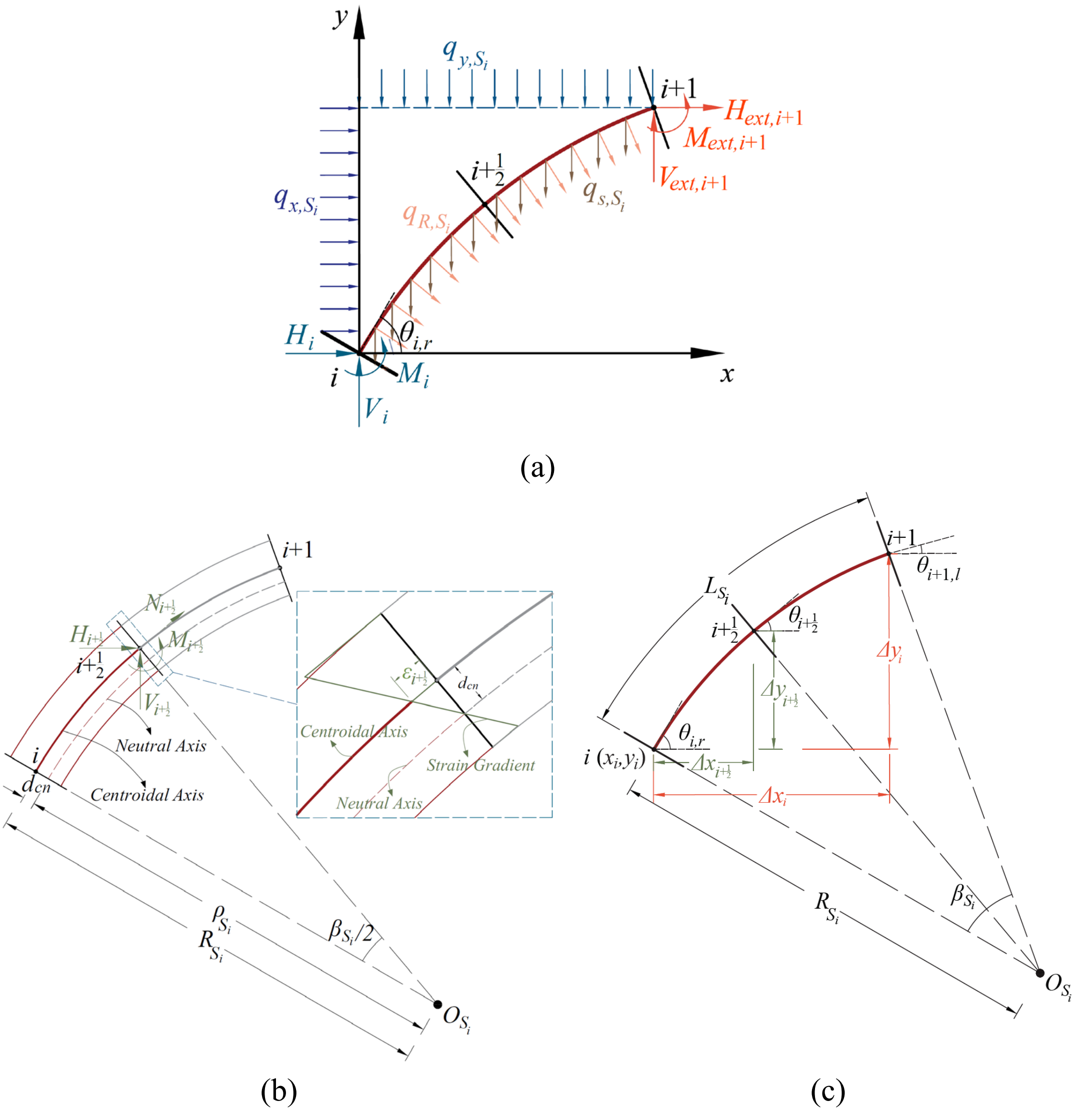

Figure 2. Illustration of the deflection function: (a) Applied loads; (b) Midpoint determination; (c) Deformed segment shape.

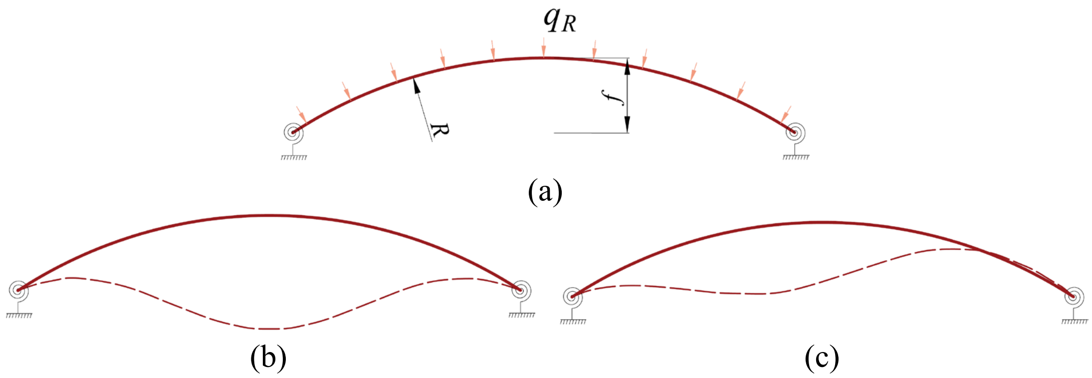

Figure 3. Illustration of a circular arch subjected to a uniform radial pressure: (a) Arch configuration and loading condition; (b) Symmetric snap-through buckling mode; (c) Anti-symmetric bifurcation buckling mode.

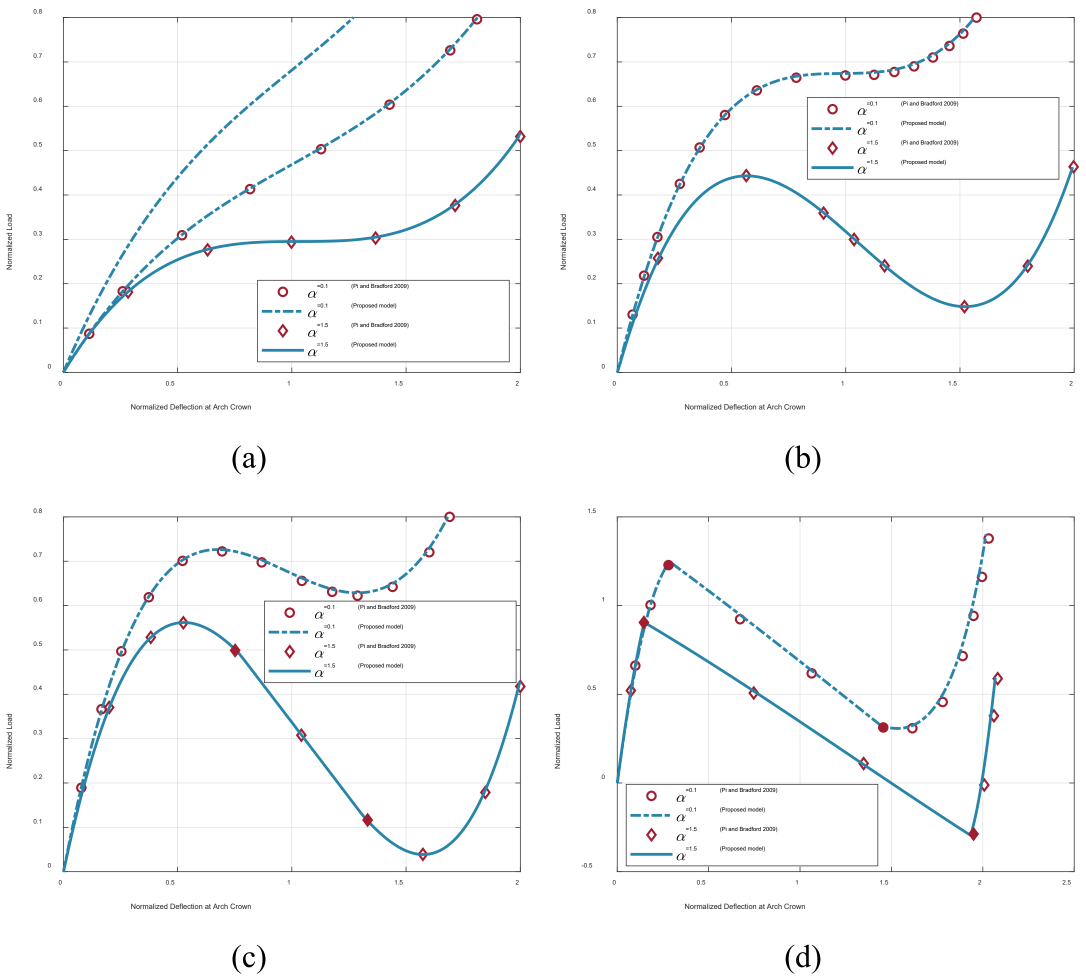

Figure 4. Results of analytical verification: (a) λ=4.35924; (b) λ=7.1431; (c) λ=8.5; (d) λ=16.

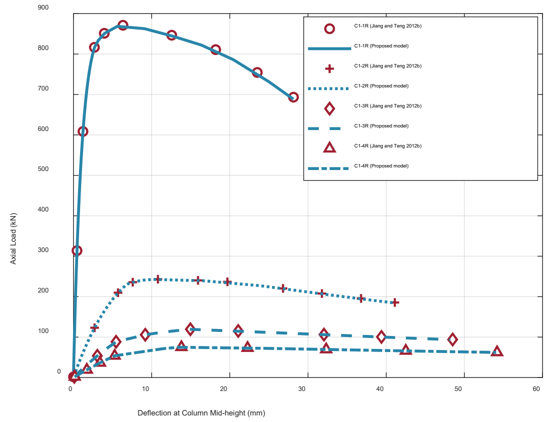

Figure 5. Results of numerical verification.

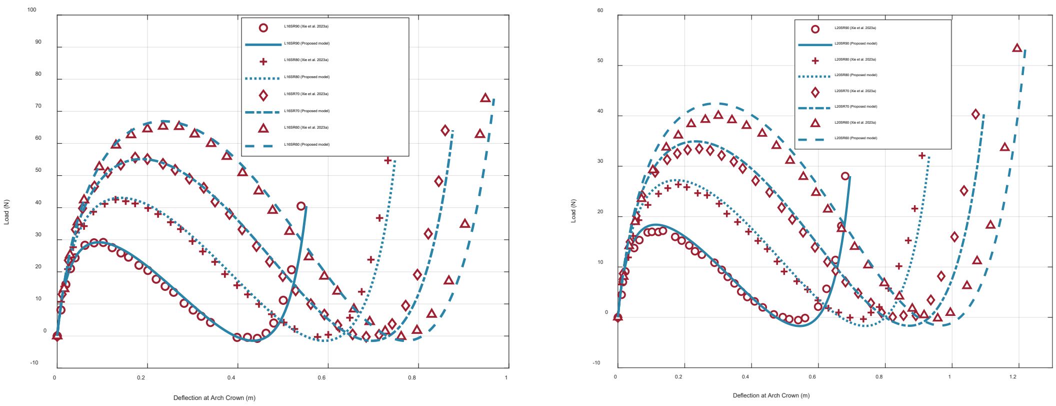

(a) (b)

Figure 6. Comparisons with load–deflection curves of FRP bending-active arches: (a) L16 specimens; (b) L20 specimens.

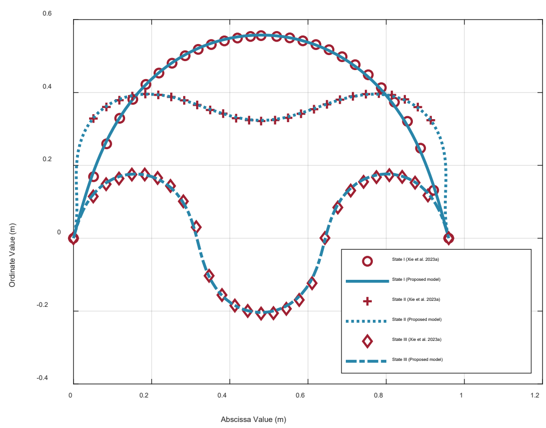

Figure 7. Comparisons with deflected shapes of Specimen L16SR60.

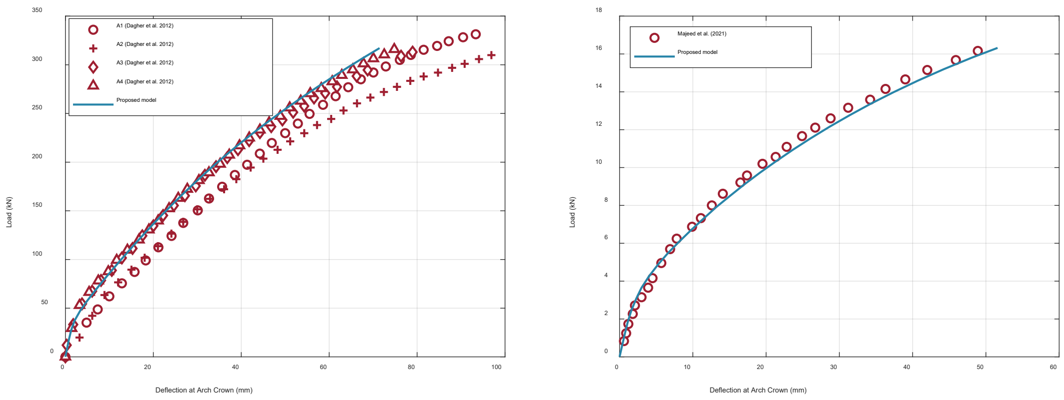

(a) (b)

Figure 8. Comparisons with load–deflection curves of CFFT arches: (a) hinge-supported; (b) fixed.